A. VINDIGNI[1]
A. RETTORI[1]
M.G. PINI[2]
C. CARBONE[3]
P. GAMBARDELLA[4],✉

Finite-sized Heisenberg chains and magnetism of one-dimensional metal systems

[1] Dipartimento di Fisica and INFM, Università di Firenze, 50019 Sesto Fiorentino, Italy
[2] Istituto dei Sistemi Complessi, Consiglio Nazionale delle Ricerche, 50019 Sesto Fiorentino, Italy
[3] Istituto di Struttura della Materia, Consiglio Nazionale delle Ricerche, 34012 Trieste, Italy
[4] Institut de Physique des Nanostructures, Ecole Polytechnique Fédérale de Lausanne, 1015 Lausanne, Switzerland

ABSTRACT We present a combined experimental and theoretical study of the magnetization of one-dimensional atomic cobalt chains deposited on a platinum surface. We discuss the intrinsic magnetization parameters derived by X-ray magnetic circular dichroism measurements and the observation of ferromagnetic order in one dimension in connection with the presence of strong, dimensionality-dependent anisotropy energy barriers of magnetocrystalline origin. An explicit transfer matrix formalism is developed to treat atomic chains of finite length within the anisotropic Heisenberg model. This model allows us to fit the experimental magnetization curves of cobalt monatomic chains, measured parallel to the easy and hard axes, and provides values of the exchange coupling parameter and the magnetic anisotropy energy consistent with those reported in the literature. The analysis of the spin–spin correlation as a function of temperature provides further insight into the tendency to magnetic order in finite-sized one-dimensional systems.

PACS 57.10.Pq; 75.30.-m; 75.30.Gw; 78.70.Dm

1 Introduction

The dimensionality of a magnetic lattice is known to affect its thermodynamic properties and in particular order–disorder magnetic phenomena. In the well-known cases of the Heisenberg and Ising models, the thermodynamic behavior of a one-dimensional (1D) spin chain of infinite length is characterized by the absence of long-range magnetic order at any non-zero temperature [1–3]. In the past, quasi-1D inorganic crystals have been traditionally investigated as 1D Heisenberg model systems [4, 5]; typical examples include tetramethylammonium copper and manganese chloride compounds, where Cu^{2+} and Mn^{2+} ions couple ferromagnetically or antiferromagnetically, respectively, along weakly interacting linear chains separated by intervening non-magnetic complexes [6–8]. More recently, the synthesis of molecular ferri- and ferromagnetic chain-like compounds containing magnetically anisotropic ions has allowed to realize 1D Ising model systems where the known absence of permanent magnetic order is accompanied by a slow relaxation of the magnetization [9–12], as predicted by Glauber more than 40 years ago [13].

✉ +41 21 693 3604, E-mail: pietro.gambardella@epfl.ch

In all these studies the investigation of 1D magnetic behavior has been concerned with insulating or molecular magnetic compounds, where the use of the Heisenberg and Ising models to reproduce the experimental behavior can be justified under the assumption of well-localized magnetic moments. On the other hand, 1D-like metallic systems, characterized by a larger degree of electron delocalization, are attracting increasing interest to explore both the fundamental limits and the practical magnetization properties of nanosized magnetic layers. Progress in heteroepitaxial growth methods allows us today to fabricate arrays of continuous, 1D mono- or bilayer stripes of a magnetic metal on top of a non-magnetic substrate [14–21], where the control of the system size can be pushed down to the monatomic limit [22–25]. Recently, 1D Co atomic chains deposited on Pt have been shown to sustain long-range ferromagnetic order of metastable character thanks to strong magnetic anisotropy energy barriers that effectively block the relaxation of the magnetization at sufficiently low temperature [23]. Owing to the partial delocalization of the d-electron states responsible for magnetism in these systems, however, it is not clear to what extent spin lattice models can be used to interpret their magnetic behavior. In this paper, we present a combined experimental–theoretical study aimed at understanding the properties of metal spin chains of finite size. The experimental results obtained for arrays of 1D Co chains grown on a vicinal Pt surface are reported in Sect. 2 where the magnitude of the local magnetic moments, the magnetic anisotropy, and the appearance of ferromagnetic order are discussed. In Sect. 3 we develop a transfer matrix formalism to analyze finite-sized 1D magnetic systems in the framework of the anisotropic Heisenberg model. We obtain very good agreement between the experiment and the Heisenberg model calculations for both the easy and hard axes magnetization curves, fitted with a single set of values of the exchange coupling constant J and the magnetic anisotropy energy D. Moreover, we discuss the spin–spin correlation function and the tendency to magnetic order as a function of temperature.

2 Magnetism of Co atomic chains deposited on Pt

2.1 Experimental

Co chains were grown by ultra-high-vacuum deposition of Co on a Pt(997) surface at $T = 260$ K [22]. At this temperature, surface diffusion causes the Co atoms to self-

assemble in an array of parallel 1D chains by decorating the steps of the Pt(997) substrate, situated 20.2 ± 1.5 Å apart. In the row-by-row growth regime, the thickness of the chains is proportional to the Co coverage, with monatomic chains corresponding to 0.13 ML (monolayers). The Co coverage was calibrated on Pt(111) against the onset of perpendicular remanence and the magnitude of the coercive field measured by X-ray magnetic circular dichroism (XMCD) compared with combined Kerr effect–scanning tunneling microscopy experiments, both quantities depending critically on the coverage [26]. Despite the accuracy of the coverage calibration, however, we note that the self-assembly process produces chains with a finite width distribution that reaches a maximum (± 0.6 atomic rows) for 0.5 ML Co, owing to the asynchronism of row-by-row growth on unequally spaced Pt terraces [27]. The magnetic characterization was performed by XMCD at beamline ID12B of the European synchrotron radiation facility (ESRF) in Grenoble on arrays of chains grown in situ. XMCD spectra (Fig. 1) were recorded at the Co $L_{2,3}$ edges (770–820 eV) by measuring the total yield of the photoemitted electrons for parallel (solid lines) and antiparallel (dotted lines) alignment of the applied magnetic field $\boldsymbol{B}$ with the light helicity. The sample was rotated about its polar and azimuthal axes with respect to the incident light direction in order to record the magnitude of the XMCD (i.e. the projec-

tion of the Co magnetization) along different crystal orientations as a function of $\boldsymbol{B}$.

2.2   *Local magnetic moments*

The 1D character of the chains has a striking influence on their overall magnetic behavior, on the local Co magnetic moment, and on the magnetocrystalline anisotropy. The reduced atomic coordination of the monatomic chains causes a remarkable increase of the magnitude of both the orbital and the spin magnetic moments compared to bulk Co and two-dimensional (2D) films. The orbital XMCD sum rule [28, 29] applied to the spectra in Fig. 1 shows that the orbital magnetic moment increases from $0.15 \pm 0.01 \mu_{\mathrm{B}}$/atom in a bulk-like Co film to $0.37 \pm 0.04 \mu_{\mathrm{B}}$/atom in the two-atom chains and $0.68 \pm 0.05 \mu_{\mathrm{B}}$/atom in the monatomic chains [23]. The magnitude of the XMCD effect relative to the total absorption signal also shows that the spin magnetic moment is increased with respect to the bulk value, but its precise determination is made difficult by the uncertainty in the dipolar spin moment that enters in the XMCD spin sum rule [30–33]. Local spin density calculations using a variety of approximation schemes, however, consistently indicate a Co spin moment between 2.1 and $2.3 \mu_{\mathrm{B}}$/atom [32–38]. These findings and their interpretation in terms of (de)localization of the Co $3d$
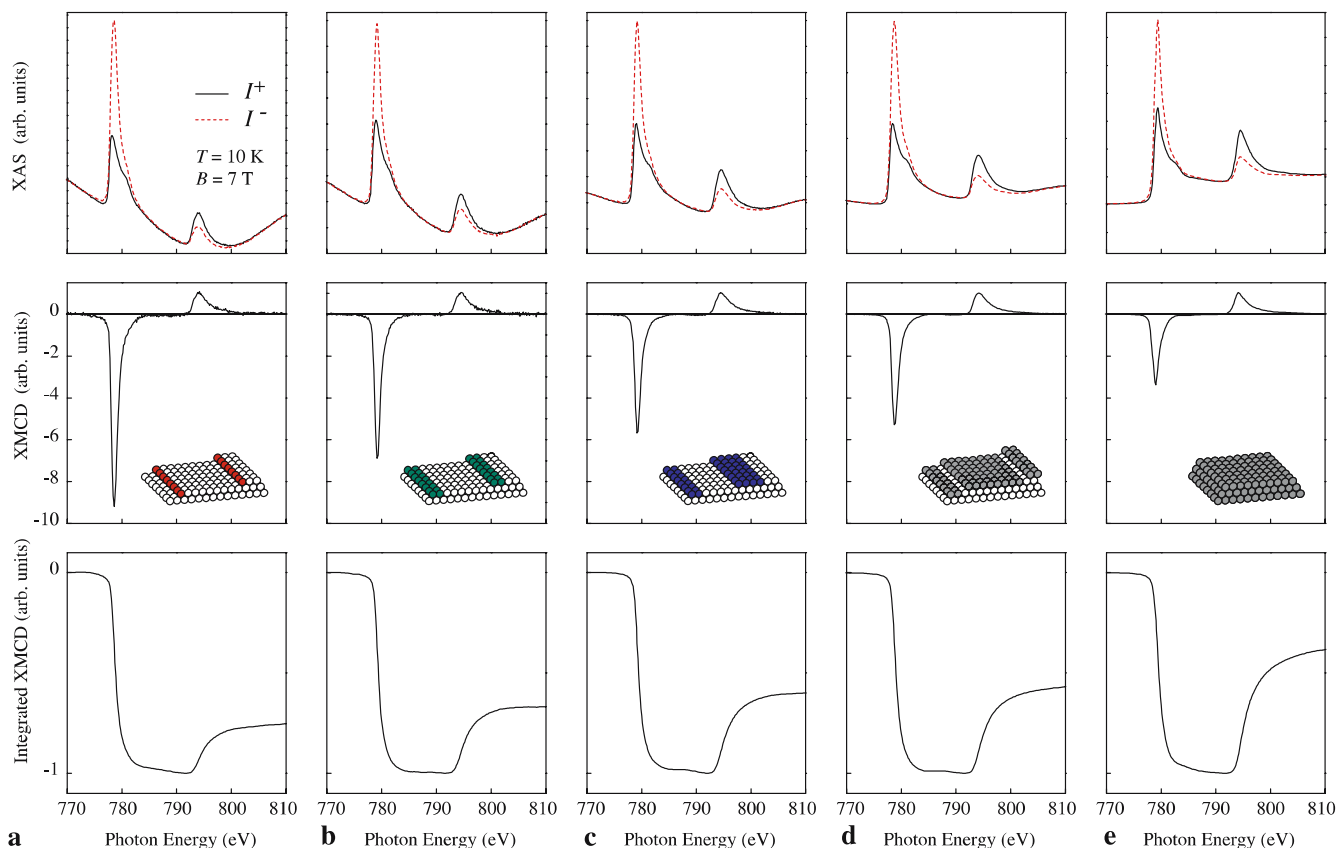

FIGURE 1 *Top*: Co X-ray absorption spectra at the $L_{2,3}$ edges for parallel (I^+) and antiparallel (I^-) directions of the light helicity and field-induced magnetization recorded at $T = 10$ K and $\boldsymbol{B} = 7$ T applied parallel to the easy magnetization direction. (**a**) Monatomic chains, (**b**) two-atom chains, (**c**) four-atom chains, (**d**) 1 ML, (**e**) bulk-like Co film (30 ML). Due to the low Co coverage, the Co absorption edges in (**a**)–(**d**) are superimposed to a strong background originating from the Pt $N_{2,3}$ thresholds. *Middle*: the dichroism signal ($I^+ - I^-$) is shown normalized to the L_2 peak to evidence changes in the relative spectral weight between the L_3 and L_2 XMCD. These changes indicate that the orbital moment increases substantially going from bulk Co to a 2D Co monolayer, and to 1D chains. *Bottom*: integrated XMCD normalized to unity at peak value

states are discussed in more detail in Refs. [23, 25, 39] and in tight-binding [40–42] as well as ab initio electronic calculations [32–38, 43, 44] relative to 1D metal systems. In the following, we intend to focus on the coupling between Co atoms in the chains and on the consequences of the strong magnetic anisotropy on the stabilization of magnetic order.

2.3   *Magnetic anisotropy and ferromagnetic order*

Figure 2 shows the magnetization of Co chains with different atomic thicknesses measured along the easy (filled symbols) and hard (open symbols) directions. Remarkably, the easy-axis direction (see the diagrams and Ref. [25]) and the magnetic anisotropy energy per Co atom present oscillations as a function of the chain thickness. This behavior appears to be specific for 1D metal systems and had been predicted by tight-binding calculations for both freestanding [40] and 1D Co chains deposited on Pd [42]. The easy axis, however, lies always in the plane perpendicular to the chains and is canted with respect to the surface normal owing to symmetry breaking at the Pt step edges [37, 38]. Dipolar interactions in the present case have a negligible strength compared to the magnetocrystalline anisotropy energy, as shown by Fig. 3 and by the out-of-plane magnetization found for a monolayer-thick Co film on Pt(997).

The magnetic response of a set of monatomic wires at $T = 45$ K (Fig. 2a) reveals zero remanent magnetization and the consequent absence of long-range ferromagnetic order. The shape of the magnetization curves, however, indicates the presence of short-range order, i.e. of significant inter-
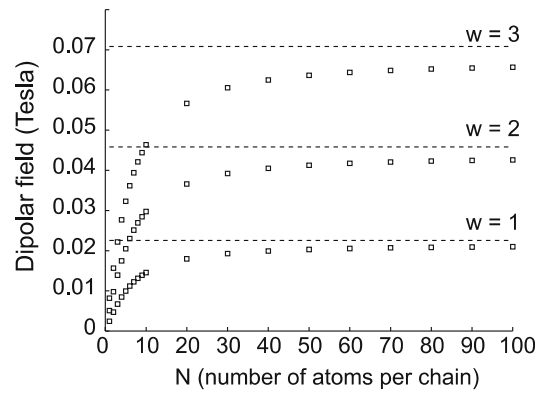

FIGURE 3   Dipolar field produced by an array of homogeneously magnetized Co chains of thickness $w = 1, 2, 3$ atoms and length N on both sides of a chain in the middle of the array. The *dashed lines* refer to chains of infinite length calculated according to Eq. (7) in Ref. [45], while the points are for discrete chains containing a finite number of atoms. The demagnetizing energy per Co atom can be calculated by multiplying the dipolar field by the Co magnetic moment (e.g. for the monatomic chains we obtain about 0.004 meV/Co atom)

atomic exchange coupling in the chains. The observed behavior is that of a 1D superparamagnetic system, i.e. a system composed by segments, or spin blocks, each containing N_c exchange-coupled Co atoms, whose resultant magnetization orientation is not stable due to thermal fluctuations. Further, the significant dependence of the magnetization on the direction of the applied field indicates a very strong magnetic anisotropy. These two observations can be taken into account in a classical picture, where the magnetic energy of the system
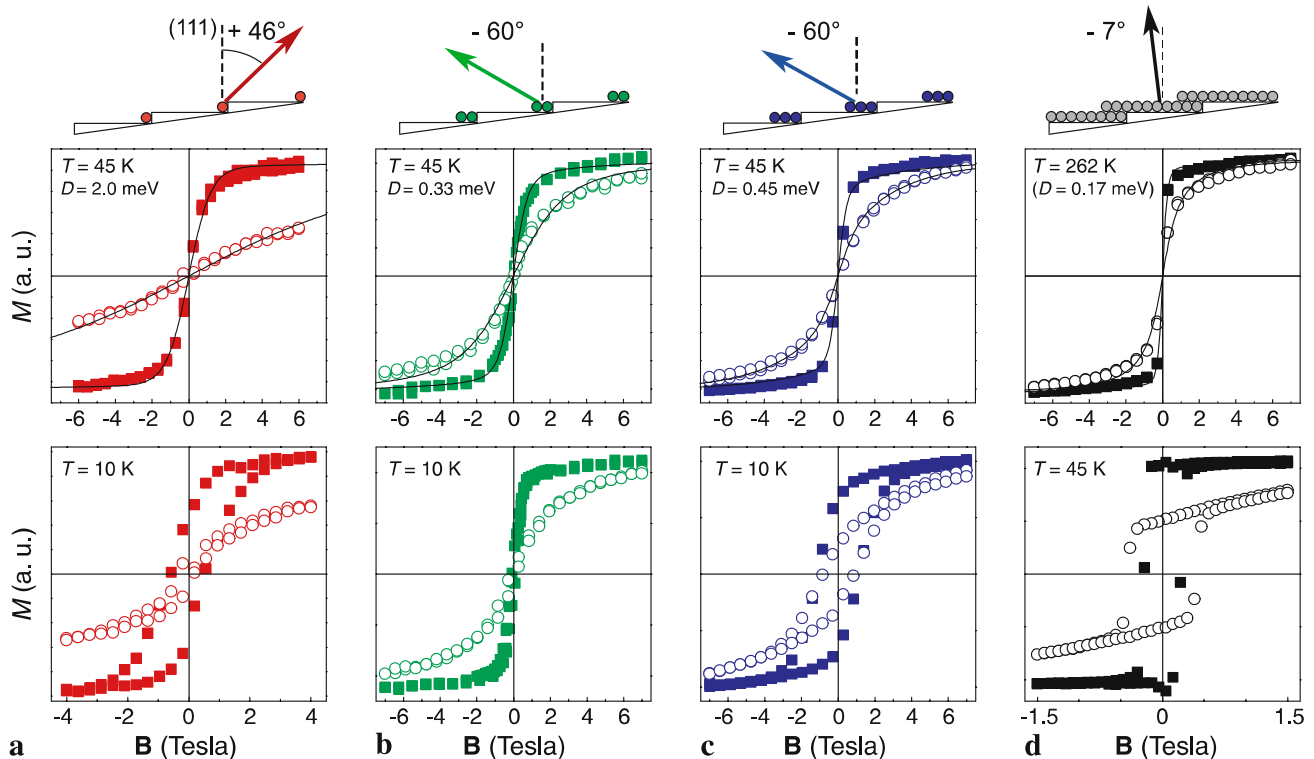

FIGURE 2   Magnetization of (**a**) monatomic, (**b**) biatomic, (**c**) triatomic chains, and (**d**) 1.3 ML Co on Pt(997) along the easy and hard directions (*filled and open symbols*, respectively), measured above and below the blocking temperature. The easy axis is indicated by the *arrows* in the *top diagrams*. The data points represent the XMCD at the L_3 Co edge (779 eV) normalized by the L_3 absorption edge jump. *Solid lines* are fits to the data according to Eq. (2)

is given by the sum of Zeeman and uniaxial anisotropy energy terms:

$$E = -N_c \boldsymbol{m}\boldsymbol{B} - N_c D(\hat{\boldsymbol{m}} \cdot \hat{\boldsymbol{e}})^2 , \qquad (1)$$

where $\boldsymbol{m}$ is the magnetic moment per Co atom (varying between 3.8 and 3.1 μ_B/atom depending on the chain thickness and including the spin and orbital contributions as well as the induced magnetization on the first and second nearest Pt neighbors [46]), D the magnetic anisotropy energy per Co atom, and $\hat{\boldsymbol{e}}$ the unit vector representing the easy-axis direction. According to Boltzmann statistics, the magnetization of an assembly of aligned chains with the easy axis oriented at an angle θ_0 with respect to $\boldsymbol{B}$ is given by

$$M = M_s \frac{\int_0^{2\pi} d\varphi \int_0^\pi d\theta \sin\theta \cos\theta \exp[-E(\theta_0, \theta, \varphi)/kT]}{\int_0^{2\pi} d\varphi \int_0^\pi d\theta \sin\theta \exp[-E(\theta_0, \theta, \varphi)/kT]} , \qquad (2)$$

where θ and φ are the polar and azimuthal spherical coordinates of $\boldsymbol{m}$ in the reference system defined by $\boldsymbol{B}$, and M_s the saturation magnetization. The simultaneous numerical fit of the easy- and hard-axes magnetization according to Eq. (2) (solid lines in Fig. 2) allows us to obtain both N_c and D [23, 25]. For the monatomic chains we find $N_c = 15$ atoms, giving an average estimate of the extent of short-range ferromagnetic order at 45 K, and $D = 2.0 \pm 0.2$ meV/Co atom. N_c turns out to be considerably smaller than the average length N of the Co chains, which is estimated to be about 80 atoms from the extension of the atomically straight sections of the Pt steps that serve as deposition template.

The fit shows that the magnetic anisotropy energy of the 1D chains is one to two orders of magnitude larger compared to typical values in 2D films [47, 48], a consequence of the reduced coordination and unquenched orbital magnetization of the Co atoms in the chains [49]. Such strong magnetic anisotropy plays a major role in stabilizing ferromagnetism in 1D, in particular to inhibit the fluctuations that lead to the zero-remanence thermodynamic limit expected for 1D systems. As in bulk ferromagnets, in fact, anisotropy energy barriers tend to maintain the magnetization along a fixed direction in space; by lowering the sample temperature below 15 K, we observe a transition to a ferromagnetically ordered state with finite remanence (Fig. 2a, bottom panel). The threshold temperature is the so-called blocking temperature, where the magnetization of each spin chain aligns along the common easy-axis direction and the system becomes ferromagnetic on a macroscopic scale. Long-range order in 1D metal chains therefore appears as a metastable state thanks to slow magnetic relaxation. As the system evolves towards a 2D film and the number of exchange-coupled Co atoms increases (Fig. 2b to d), we expect a stronger tendency towards magnetic order. Contrary to expectations, however, in the two-atom chains we observe vanishing long-range magnetic order even at low temperature (Fig. 2b bottom panel). In this case, the tendency towards order is counteracted by the drastic reduction of the magnetic anisotropy energy per Co atom. Paradoxically, therefore, the 1D character of the monatomic chains favors rather than disrupts ferromagnetic order owing to the minimal coordination of the Co atoms and related enhanced magnetic anisotropy energy.

We note further that, although generally much lower compared to the monatomic case, D changes in a non-monotonic way with the chain thickness (Fig. 2). This effect, which is accompanied also by oscillations of the easy magnetization axis [25], is related to the specific electronic configuration of Co chains formed by one or more adjacent atomic rows [40].

In the following sections, we will compare the results of the above analysis for the monatomic chains with those expected for finite 1D spin chains in the framework of the anisotropic Heisenberg model. A consistent picture of 1D metal systems can be obtained while gaining more insight into the spin arrangement at the microscopic level.

3 Finite-sized spin chains in the anisotropic Heisenberg model

3.1 *The finite-size transfer matrix*

To study the static properties of the Co chains described in Sect. 2, we employ the transfer matrix approach [50, 51] for the anisotropic Heisenberg model that we adapt to the case of a 1D system of finite length. We describe first the derivation of the transfer kernel and of the free energy of the system, then the average spin magnetization and the two-spin correlation function. We consider a spin chain of length N with free boundary conditions (no translational invariance). A general spin Hamiltonian with only nearest-neighbor interaction takes the form

$$\mathcal{H} = -\sum_{i=1}^{N-1} V_0(\boldsymbol{S}_i, \boldsymbol{S}_{i+1}) - \sum_{i=1}^{N} V_{ss}(\boldsymbol{S}_i) , \qquad (3)$$

where we separate the single-spin contribution $V_{ss}(\boldsymbol{S}_i)$ (single-spin anisotropy, Zeeman term, etc.) from the exchange term $V_0(\boldsymbol{S}_i, \boldsymbol{S}_{i+1})$ [52–54]. The transfer kernel can be defined as follows:

$$\mathcal{K}(\boldsymbol{S}_i, \boldsymbol{S}_{i+1})$$
$$= \exp\left[\beta V_0(\boldsymbol{S}_i, \boldsymbol{S}_{i+1}) + \frac{1}{2}\beta(V_{ss}(\boldsymbol{S}_i) + V_{ss}(\boldsymbol{S}_{i+1})) \right] , \qquad (4)$$

with β the inverse temperature in Boltzmann units. $\mathcal{K}$ is related to the partition function through

$$\mathcal{Z}_N = \int d\Omega_1 \int d\Omega_2 \dots \int \mathcal{K}(\boldsymbol{S}_1, \boldsymbol{S}_2) \dots \mathcal{K}(\boldsymbol{S}_{N-1}, \boldsymbol{S}_N)$$
$$\times \exp\left[\frac{1}{2}\beta(V_{ss}(\boldsymbol{S}_1) + V_{ss}(\boldsymbol{S}_N)) \right] d\Omega_N . \qquad (5)$$

For the simplest systems the kernel (4) is symmetric in the exchange $\boldsymbol{S}_i \leftrightarrow \boldsymbol{S}_{i+1}$. The static properties of the model defined by the Hamiltonian (3), as well as the partition function itself, can be better handled by solving the integral eigenvalue problem

$$\int d\Omega_{i+1} \mathcal{K}(\boldsymbol{S}_i, \boldsymbol{S}_{i+1})\psi_m(\boldsymbol{S}_{i+1}) = \lambda_m \psi_m(\boldsymbol{S}_i) , \qquad (6)$$

where λ_m are the eigenvalues corresponding to the (right-hand) eigenfunctions ψ_m. If the kernel was not symmetric with respect to $\boldsymbol{S}_i$ and $\boldsymbol{S}_{i+1}$, as in the case of heterogeneous

magnetic neighbors, an additional integral equation would be necessary to obtain the left-hand eigenfunctions. The infinite-dimensional space defined by the eigenfunctions of Eq. (6), under very general hypotheses, fulfills the completeness and orthonormality relationships

$$\sum_m \psi_m(S_i)\psi_m(S_j) = \delta(S_i - S_j) ,\qquad(7)$$

$$\int \psi_n(S)\psi_m(S)\,\mathrm{d}\Omega = \delta_{n,m} ,\qquad(8)$$

respectively, where $\delta(S_i - S_j)$ is the Dirac δ-function and $\delta_{n,m}$ the Kronecker symbol. Using the completeness property (7), the kernel can be rewritten as

$$\mathcal{K}(S_i, S_{i+1}) = \sum_m \lambda_m \psi_m(S_i)\psi_m(S_{i+1}) .\qquad(9)$$

The eigenvalues λ_m are all real and positive, as the kernel operator (4) is a positive function of S_i and S_{i+1}. In the symmetric case, i.e. $\mathcal{K}(S_i, S_{i+1}) = \mathcal{K}(S_{i+1}, S_i)$, the reality of the eigenvalues follows from the analogue of the spectral theorem for real symmetric matrices; furthermore, it is possible to show that the spectrum of the eigenproblem (6) is upper bounded: thus, the eigenvalues λ_m can be ordered from the largest to the smallest one:

$$\lambda_0 > \lambda_1 > \lambda_2 > \dots$$

Putting the kernel in the form (9) and exploiting the orthonormality (8), we obtain

$$\mathcal{Z}_N = \sum_m \lambda_m^{N-1} a_m^2 \quad \text{with}\qquad(10)$$

$$a_m = \int \exp\left[\frac{1}{2}\beta(V_{ss}(S_i))\right] \psi_m(S_i)\,\mathrm{d}\Omega_i .$$

If the reader is familiar with the infinite chain transfer matrix formalism [55], he will appreciate that in the present study the knowledge of the whole spectrum is required even for the computation of the partition function $\mathcal{Z}_N$, while in the thermodynamic limit the latter is simply given by

$$\mathcal{Z}_\infty \underset{N\to\infty}{\sim} \lambda_0^N .\qquad(11)$$

The dependence on the a_m integral also represents a remarkable difference. The free energy, given by the fundamental relation

$$F_N = -k_B T \ln \mathcal{Z}_N ,\qquad(12)$$

can be usefully written as

$$F_N = -\beta^{-1}$$
$$\times \left\{ N \ln \lambda_0 + \ln\left(\frac{a_0^2}{\lambda_0}\right) + \ln\left[1 + \sum_{m\neq 0}\left(\frac{a_m}{a_0}\right)^2\left(\frac{\lambda_m}{\lambda_0}\right)^{N-1}\right]\right\} .\qquad(13)$$

In the first term, proportional to the length of the chain, one recognizes the 'bulk' contribution, identical to the free energy of the infinite chain; the second, independent of N, is the 'surface' term, responsible just for the end-point behavior; the third is the finite-size contribution which decays exponentially with increasing length of the segment. In the thermodynamic limit, of course, only the 'bulk' contribution survives. From the derivatives of the free energy (13) several thermodynamic observables may be obtained, which will also be characterized by bulk, surface, and finite-size contributions. In particular, the average of the spin components and the size dependence of the magnetization will be discussed in Sects. 3.3 and 3.5.

3.2 Sampling of the solid angle

Equation (6), yielding the eigenvalues λ_m and the eigenfunctions ψ_m as a preliminary step to the evaluation of any physical quantity within the transfer matrix scheme, encompasses an integration over the unitary sphere. Other integrations of the same kind are required to compute the average of the spin components (18) and the spin–spin correlation function (22) that will be introduced later. Given a generic function of two angles θ and φ, say $f(\theta, \varphi)$, the integral over the whole solid angle 4π may be approximated as

$$\int f(\varphi, \theta)\,\mathrm{d}\Omega \simeq \sum_{h=1}^{P} w_h f(u_h) \quad \text{with} \quad \mathrm{d}\Omega = \mathrm{d}\varphi\sin\theta\,\mathrm{d}\theta ,$$

where u_h represent the P special points that sample the unitary sphere and w_h their relative weights [56]. Several samplings of the unitary sphere are reported in the literature, which are characterized by a total number of points P and relative weights that fulfill certain optimization criteria. In terms of such a discretization the transfer kernel eigenvalue problem (6) becomes

$$\sum_{h=1}^{P} w_h \mathcal{K}(u_l, u_h)\,\psi_m(u_h) = \lambda_m \psi_m(u_l) ,\qquad(14)$$

which, after the symmetrization

$$\begin{cases} K_{l,h} &= \sqrt{w_l w_h}\,\mathcal{K}(u_l, u_h) ,\\ \Psi_h^n &= \sqrt{w_h}\,\psi_n(u_h) \end{cases}$$

is usually rewritten as

$$\sum_{h=1}^{P} K_{l,h}\Psi_h^n = \lambda_n \Psi_l^n .\qquad(15)$$

As one can see, sampling the solid angle transforms the integral equations (6) into a linear algebra symmetric problem, which can be solved using one of the existing routines (DSPEV of the LAPACK package [57], for example). This also implies that the number of eigenvalues is reduced to the actual number of special points P (with respect to the continuous variable formulation in which the number of λ is infinite). In the following calculations we employ the Gauss spherical product formula of 16th degree [58] ($P = 200$). With this choice, the numerical results agree with the analytical estimation of the largest eigenvalue λ_0 given by Fisher [59] for the Heisenberg isotropic model in zero field up to the most significant digit for $\beta J < 10$ (see Eq. (24) in the following).

3.3   *Average of the spin components*

The average of the α component of spin i is given by

$$\langle S_i^\alpha \rangle = \frac{1}{\mathcal{Z}_N} \int d\Omega_1 \int d\Omega_2 \dots \int \mathcal{K}(S_1, S_2) \dots \mathcal{K}(S_{i-1}, S_i)$$
$$\times S_i^\alpha \, \mathcal{K}(S_i, S_{i+1}) \dots \mathcal{K}(S_{N-1}, S_N)$$
$$\times \exp\left[\frac{1}{2}\beta\left(V_{ss}(S_1) + V_{ss}(S_N)\right)\right] d\Omega_N . \tag{16}$$

As translational invariance does not hold, we expect this quantity to vary from site to site, while the index i represents only a dummy variable for the infinite chain. Exploiting the identity (9) for the kernel and the orthonormality relations (8), we have

$$\langle S_i^\alpha \rangle = \frac{1}{\mathcal{Z}_N}$$
$$\times \sum_{m_1, m_2 \dots, m_{N-1}} \lambda_{m_1} \lambda_{m_2} \dots \lambda_{m_{N-1}} \delta_{m_1, m_2} \delta_{m_2, m_3} \dots \delta_{m_{i-2}, m_{i-1}}$$
$$\times \int \psi_{m_{i-1}}(S_i) S_i^\alpha \psi_{m_i}(S_i) \, d\Omega_i \delta_{m_i, m_{i+1}} \dots \delta_{m_{N-2}, m_{N-1}}$$
$$\times \int \psi_{m_1}(S_1) \exp\left[\frac{1}{2}\beta V_{ss}(S_1)\right] d\Omega_1 \int \exp\left[\frac{1}{2}\beta V_{ss}(S_N)\right]$$
$$\times \psi_{m_{N-1}}(S_N) \, d\Omega_N , \tag{17}$$

from which, accounting for all the Kronecker symbols,

$$\langle S_i^\alpha \rangle = \frac{1}{\mathcal{Z}_N} \sum_{m_1 m_{N-1}} \lambda_{m_1}^{i-1} a_{m_1} B_{m_1 m_{N-1}}^\alpha a_{m_{N-1}} \lambda_{m_{N-1}}^{N-i}$$
$$\text{for} \quad 2 \le i \le N-1$$
$$\text{with} \quad B_{mn}^\alpha = \int \psi_m(S_i) S_i^\alpha \psi_n(S_i) \, d\Omega_i . \tag{18}$$

The chosen site i index appears in the exponent of the eigenvalues (λ_{m_1} and $\lambda_{m_{N-1}}$) and weights the contribution of each term in the sum (18) in a different way [60]. Equation (18), as usual, furnishes an alternative route to compute the magnetization rather than using the logarithmic derivative of $\mathcal{Z}_N$; in fact, the α component of the total magnetization corresponds to

$$M_N^\alpha = \frac{g}{N} \sum_{i=1}^N h_\gamma^\alpha \langle S_i^\gamma \rangle , \tag{19}$$

where g is the gyromagnetic factor and h_γ^α gives the directors of the external field with respect to the spin frame, taking the sum over the repeated γ index.

3.4   *The spin–spin correlation matrix*

α and γ being the considered components of the ith and the $(i+r)$th spins, respectively, the two-spin correlation function is given by

$$\langle S_i^\alpha S_{i+r}^\gamma \rangle = \frac{1}{\mathcal{Z}_N} \int d\Omega_1 \int d\Omega_2 \dots \int \mathcal{K}(S_1, S_2) \dots$$
$$\mathcal{K}(S_{i-1}, S_i) S_i^\alpha \mathcal{K}(S_i, S_{i+1}) \dots \mathcal{K}(S_{i+r-1}, S_{i+r}) S_{i+r}^\gamma$$
$$\times \mathcal{K}(S_{i+r}, S_{i+r+1}) \dots \mathcal{K}(S_{N-1}, S_N)$$
$$\times \exp\left[\frac{1}{2}\beta\left(V_{ss}(S_1) + V_{ss}(S_N)\right)\right] d\Omega_N . \tag{20}$$

Exploiting the kernel definition (9) and the orthonormality relations (8), we obtain

$$\langle S_i^\alpha S_{i+r}^\gamma \rangle = \frac{1}{\mathcal{Z}_N}$$
$$\times \sum_{m_1, m_2 \dots, m_{N-1}} \lambda_{m_1} \lambda_{m_2} \dots \lambda_{m_{N-1}} \delta_{m_1, m_2} \delta_{m_2, m_3} \dots \delta_{m_{i-2}, m_{i-1}}$$
$$\times \int \psi_{m_{i-1}}(S_i) S_i^\alpha \psi_{m_i}(S_i) \, d\Omega_i \delta_{m_i, m_{i+1}} \dots \delta_{m_{i+r-2}, m_{i+r-1}}$$
$$\times \int \psi_{m_{i+r-1}}(S_{i+r}) S_{i+r}^\gamma \psi_{m_{i+r}}(S_{i+r}) \, d\Omega_{i+r} \delta_{m_{i+r}, m_{i+r+1}} \dots$$
$$\times \delta_{m_{N-1}, m_N} \int \psi_{m_1}(S_1) \exp\left[\frac{1}{2}\beta V_{ss}(S_1)\right] d\Omega_1$$
$$\times \int \exp\left[\frac{1}{2}\beta V_{ss}(S_N)\right] \psi_{m_{N-1}}(S_N) \, d\Omega_N . \tag{21}$$

Considering all the repeated indices in the Kronecker symbols, we finally obtain

$$\langle S_i^\alpha S_{i+r}^\gamma \rangle = \frac{1}{\mathcal{Z}_N}$$
$$\times \sum_{m_1 m_i m_{N-1}} \lambda_{m_1}^{i-1} a_{m_1}^\dagger B_{m_1 m_i}^\alpha \lambda_{m_i}^r B_{m_i m_{N-1}}^\gamma a_{m_{N-1}} \lambda_{m_{N-1}}^{N-i-r}$$
$$\text{for} \quad 2 \le i \le N-1 . \tag{22}$$

As the average of the spin components computed above, the spin–spin correlation function (22) depends on both the chosen sites i and $i+r$ in chains of finite length [60]. This function can be conveniently represented by means of a matrix:

$$\mathcal{C}_{i,i+r}^{\alpha\gamma} = \langle S_i^\alpha S_{i+r}^\gamma \rangle , \tag{23}$$

real and symmetric in the exchange $i \leftrightarrow i+r$ and $i \leftrightarrow N-i$, for obvious physical reasons. Further, the diagonal terms (with $r=0$) give the static autocorrelation function and correspond to the maxima line of the matrix elements $\mathcal{C}_{i,i+r}^{\alpha\gamma}$. In general, the off-diagonal terms as well as the diagonal ones depend on the temperature, and the farther a term lies from the diagonal the smaller its value is. In this sense the three-dimensional (3D) plot of the matrix (23) can be pictorially imagined as a square 'cloth' hanging on a diagonal string (the maxima line) with a temperature-dependent slope. In the infinite-temperature limit the off-diagonal terms vanish, leaving just the diagonal string contribution. In the zero-temperature limit the matrix degenerates into a flat surface. In Fig. 4 one of the matrices $\mathcal{C}_{i,j}^{\alpha\alpha}$ is reported for the isotropic Heisenberg model in zero field:

$$\mathcal{H} = -\sum_{i=1}^{N-1} J S_i S_{i+1}, \quad |S_i|^2 = 1 , \tag{24}$$

a $\beta J = 20$

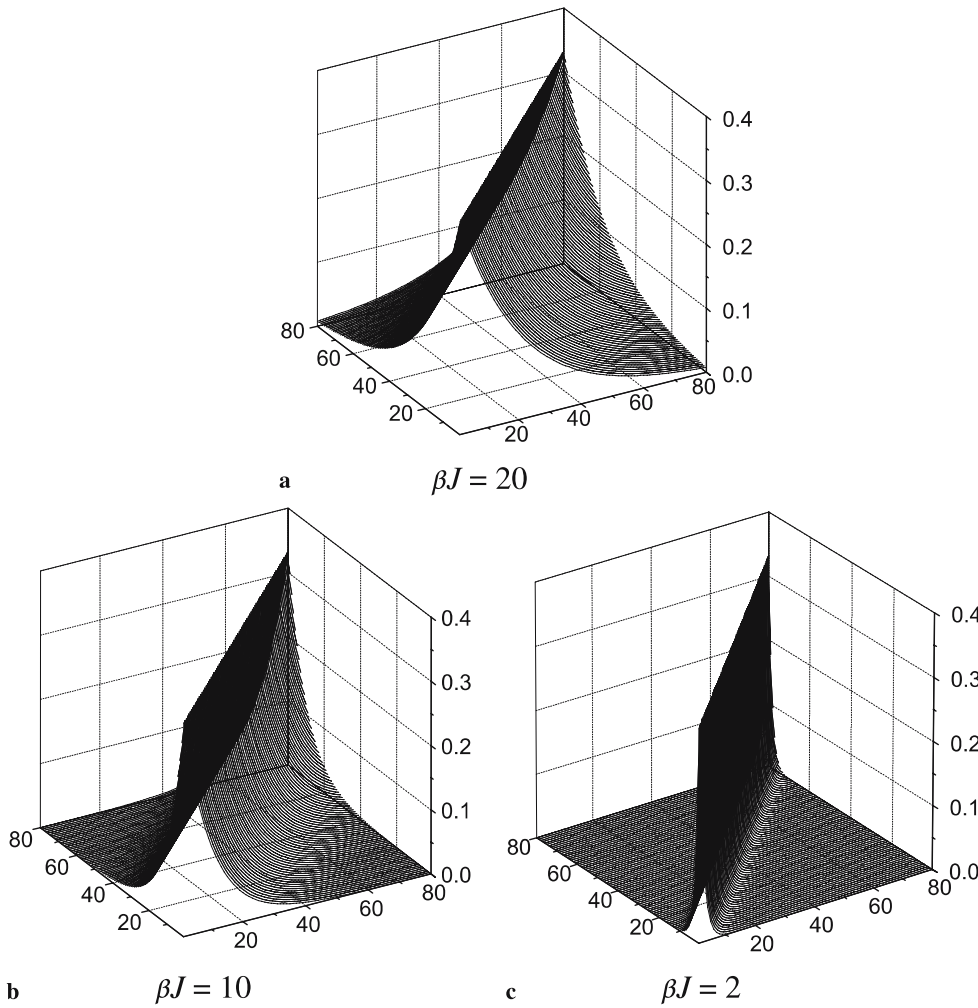**b** $\beta J = 10$

c $\beta J = 2$

FIGURE 4 Correlation matrix of the isotropic Heisenberg model with open boundary conditions and $N = 80$ spins: the basal plane represents the considered couples of spin (i, j); the corresponding correlation function $\mathcal{C}_{i,j}^{\alpha\alpha}$ is reported on the *vertical axis*

with $N = 80$ for different inverse reduced temperatures βJ; in this particular case the three matrices ($\alpha = x, y, z$) $\mathcal{C}_{i,j}^{\alpha\alpha}$ are equal, thanks to the rotational symmetry of the Heisenberg Hamiltonian (24), while the other six matrices are zero, as the mixed spin components ($\alpha \neq \gamma$) are not correlated. The diagonal values are equal to $\frac{1}{3}$ at any temperature (unitary spins are considered). In the zero-temperature limit, the off-diagonal terms also reach the same value, as $\mathcal{C}_{i,j}^{\alpha\alpha}$ degenerates into a flat surface: the system becomes essentially a rigid block of N spins (classical Heisenberg model ground state). In the sequence a, b, c of Fig. 4 the $\mathcal{C}_{i,j}^{\alpha\alpha}$ matrix is reported for decreasing values of the variable βJ. For $\beta J = 20$ the $\mathcal{C}_{i,j}^{\alpha\alpha}$ extremes are appreciably 'detached' from the zero plane, revealing a correlation even between the farthest spins. Raising the temperature (reducing βJ) reduces the correlation between the farthest spins as the correlation matrix tends towards a family of Dirac δ-functions centered on the diagonal terms (Fig. 4c).

3.5 *Fit of the experimental Co chain magnetization*

The magnetization of the monatomic chains presented in Sect. 2.3 can now be fitted using the finite-size transfer matrix algorithm implemented with the sampling of the solid angle by means of Eqs. (18) and (19). This the-oretical approach cannot account for dynamic effects, but only allows us to calculate the thermodynamic and static behavior of a classical spin lattice. Therefore, we fit only the reversible magnetization curves obtained at $T = 45$ K. The model Hamiltonian in the present case is

$$\mathcal{H} = -\sum_{i=1}^{N-1} J S_i S_{i+1} - \sum_{i=1}^{N} \left[D\left(S_i^z\right)^2 + g_{\text{Co-Pt}} \mu_\text{B} B S_i \right] , \quad (25)$$

where J is the exchange coupling constant and $|S_i|^2 = 1$. The gyromagnetic factor $g_{\text{Co-Pt}}$ has been set equal to 3.8 to take into account the Co spin and orbital atomic moment as well as the induced moment on Pt (see Sect. 2.2). We have chosen $N = 80$ as suggested by the structural analysis of the Pt(997) surface. This value of N is shown in the following to give consistent results with both the experiment and first-principles calculations of the magnetic anisotropy energy. We point out, however, that the actual 'magnetic' length of the chains can also be influenced by dislocations, substitutional impurities, and contaminants that can never be completely eliminated in the experiment [22, 61]. The free parameters in the fit are thus the J and D constants and a rescaling factor for the magnetization, since the XMCD curves in Fig. 2 are given in arbitrary units. Figure 5 shows the fit performed on the magnetization data measured along both the easy and hard directions at
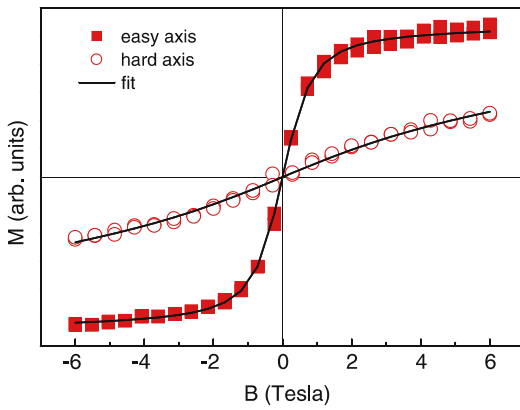
FIGURE 5 Heisenberg model fit (*solid lines*) of the experimental magnetization measured at $T = 45$ K parallel to the easy axis (*solid squares*) and 80° off the easy axis (*empty circles*), assuming $N = 80$

herent differences between the model used to fit the Co chain magnetization in Sect. 2.3 and the present calculation, we find consistent results for the uniaxial magnetic anisotropy energy term. Electronic structure calculations for Co monatomic chains deposited on Pt [33, 35–38] also agree with our results. The larger D found for the Heisenberg fit with respect to Eq. (2) can be explained by the assumption of rigid spin blocks in the latter model. Using the fit parameters derived above, we can now investigate magnetic correlation effects along our model Co chains at different temperatures. Figure 6a and b show the correlation matrices $\mathcal{C}_{i,j}^{zz}$ and $\mathcal{C}_{i,j}^{xx}$ for the Hamiltonian (25) in zero field at $T = 45$ K. The zz correlation at this temperature is already quite strong between all the spins of the chain, as the matrix values are rather detached from the zero plane away from the diagonal terms. One can notice also that the FWHM of the correlation function cut across the diagonal corresponds to the average size of the spin block estimated in Sect. 2.3. Excluding the end spins, the spin–spin diagonal correlation for the easy-axis matrix $\mathcal{C}_{i,j}^{zz}$ is about three times larger compared to $\mathcal{C}_{i,j}^{xx}$, reflecting the anisotropy of the system. Also, the hard-plane correlation (the results obtained for $\mathcal{C}_{i,j}^{xx}$ and $\mathcal{C}_{i,j}^{yy}$ are identical thanks to the symmetry about the z axis of the Hamiltonian (25)) vanishes faster compared to the correlation between the easy-axis components. Typically related to the finite size of the chains is the smoothing of the diagonal maxima curve of the $\mathcal{C}_{i,j}^{zz}$ matrix in the vicinity of the
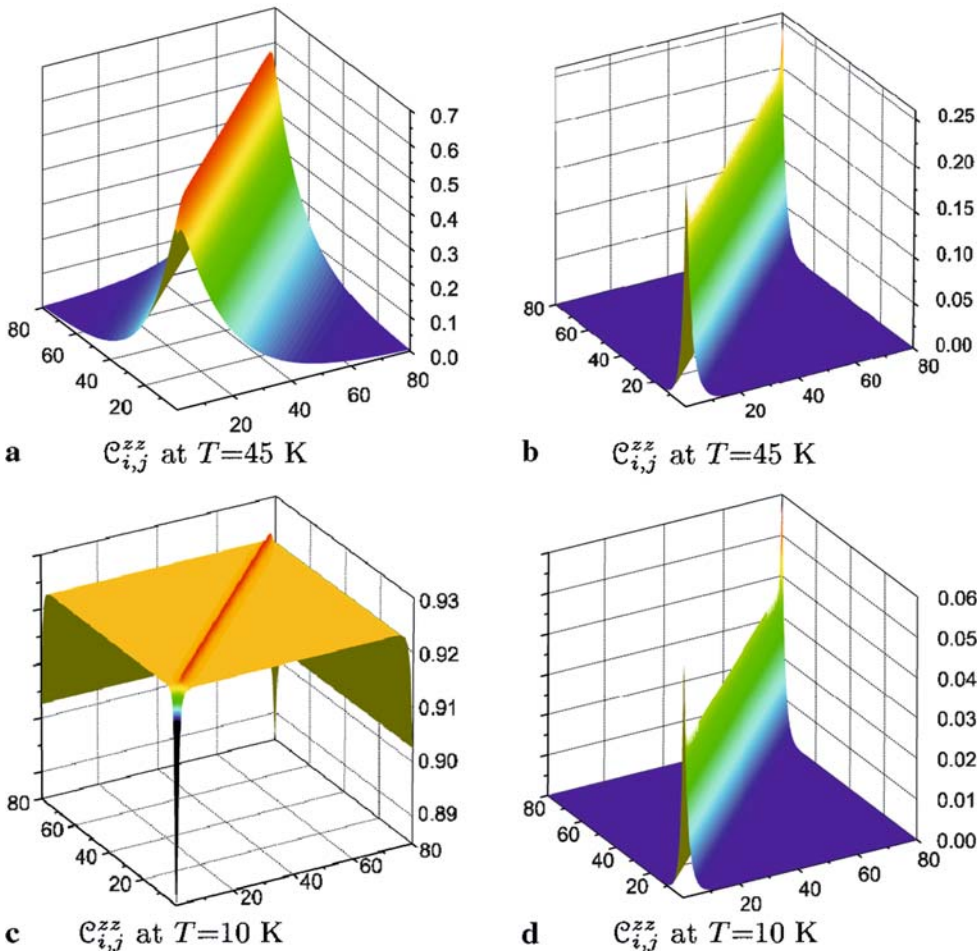
$T = 45$ K. For the two parameters of the spin Hamiltonian we obtain $J = 228.7$ K (20 meV) and $D = 38.3$ K (3.3 meV). The value of J is in agreement with first-principles calculations of the interatomic exchange interaction in bulk and monolayer Co structures ranging from 15 to 40 meV [62–64] and slightly larger than the Fe exchange coupling (14 meV) estimated for a Fe monolayer on a W(110) surface on the basis of a micromagnetic analysis [21, 65]. Notably, despite the in-

a $\mathcal{C}_{i,j}^{zz}$ at $T=45$ K

b $\mathcal{C}_{i,j}^{zz}$ at $T=45$ K

c $\mathcal{C}_{i,j}^{zz}$ at $T=10$ K

d $\mathcal{C}_{i,j}^{zz}$ at $T=10$ K

FIGURE 6 Correlation matrix of the Hamiltonian (25) computed using the fit parameters for the two experimental temperatures $T = 45, 10$ K. The basal plane represents the considered couples of spin (i, j); the correlation functions $\mathcal{C}_{i,j}^{zz}$ (**a**) and (**c**) and $\mathcal{C}_{i,j}^{xx}$ (**b**) and (**d**) are reported on the *vertical axis*

end points. The zz-autocorrelation function ($\mathcal{C}_{i,i}^{zz}$) is in fact expected to be smaller for the spins at the chain edges, as they miss one magnetic neighbor and can fluctuate more freely. Through the constraint given by the norm of each spin vector, this effect reflects on the hard-plane autocorrelation functions ($\mathcal{C}_{i,i}^{xx}$ and $\mathcal{C}_{i,i}^{yy}$) too: their values increase in the vicinity of the edges (see spikes in Fig. 6b) in order to satisfy the relationship $\langle S_i^x S_i^x \rangle + \langle S_i^y S_i^y \rangle + \langle S_i^z S_i^z \rangle = 1$. The same effect does not occur in the isotropic Heisenberg model (see Fig. 4) because the symmetry of the Hamiltonian forces the spin–spin correlation function to contribute to the same level to the unitary norm $|\boldsymbol{S}_i|^2$ and $\langle S_i^x S_i^x \rangle = \langle S_i^y S_i^y \rangle = \langle S_i^z S_i^z \rangle = \frac{1}{3}$ for any temperature and at any site. We can conclude that the localization of disorder is enhanced by the anisotropy term D, while it completely disappears in the isotropic Heisenberg limit.

At $T = 10$ K the correlation between the spins along the easy axis (Fig. 6c) is much stronger compared to 45 K. It is interesting to observe that the correlation of the first (not evident from the picture) and the last spins with all the others is significantly weaker than between the middle spins; this is again consistent with the confinement of entropy close to the end spins. The relationship between the autocorrelation function along the easy axis and those of the hard plane (Fig. 6d) is similar to that described above for $T = 45$ K. The analysis of the correlation matrix in terms of the plot of Fig. 6 reveals, even at first sight, that the physics of the system at the two considered temperatures may be very different, and supports the experimental observation of ferromagnetic order in the monatomic Co chains.

As the diagonal terms of the correlation matrix are directly related to the susceptibility, the localization of disorder at the end spins indicates that these will respond to an applied field differently from the 'bulk' spins. It is therefore possible that, depending on the length of the chains [66], thermally activated magnetization reversal will proceed in a non-uniform way from the end points towards the center of the chains [10, 67, 68]. In Fig. 7 we report the site dependence of the average easy-axis spin projection $\langle S_i^z \rangle$ in the presence of an applied field $B_z = 2$ T at $T = 45$ K. The profiles obtained for segments of different lengths N are compared with the expectation value of the infinite chain [50]. Translational invariance is broken for any segment except for the infinite chain, and $\langle S_i^z \rangle$ decreases symmetrically with respect to the middle of the segment while moving towards the end spins. It is worthwhile to note that the asymptotic value for the infinite chain is never reached for segments smaller than $N = 50$. Also, for $N < 100$ we expect the total magnetization (19) to be significantly lower compared to the infinite chain at this field. From the above discussion, it is evident that, depending on the temperature, finite-size effects play a central role in determining the magnetization of 1D systems. The finite-size transfer matrix approach allows us to take such effects into account and, by means of the correlation matrix, provides powerful physical insight beyond the information hidden in the experimental magnetization curves.

4   Conclusions

In conclusion, we have analyzed the magnetic behavior of 1D Co metal chains deposited on a vicinal Pt surface. The experimental analysis revealed a particularly rich scenario: the magnitude of the local Co magnetic moment, in particular the orbital component, is enhanced with respect to the 2D and 3D cases and depends critically on the thickness of the chains. The magnetic anisotropy energy as well as the easy axis of magnetization oscillate with chain thickness. Depending on the substrate temperature, Co monatomic chains can sustain short- or long-range ferromagnetic order of metastable character. Owing to large magnetic anisotropy energy barriers and related slow magnetic relaxation, ferromagnetism can be observed in the monatomic chains without contradicting thermodynamic restrictions to long-range magnetic order in 1D. These results have been interpreted on the basis of the 1D anisotropic Heisenberg model, which has been implemented using a finite-size transfer matrix approach to treat spin chains of finite length. The model allowed us to fit the Co monatomic chain magnetization data in the reversible limit and to extract the values of the anisotropy energy and nearest-neighbor exchange constant in the chains. The spin–spin correlation matrix calculated using these parameters provided deeper insight into the localization of order/disorder effects in the chains at different temperatures due to their finite size and the presence of magnetic anisotropy.

FIGURE 7   The site dependence of $\langle S_i^z \rangle$ is shown for different lengths of the segments at $T = 45$ K. The site index is enumerated starting from the middle of each segment (the convention of the correlation function is not followed). The *dashed line* corresponds to the infinite-chain expectation value

REFERENCES

1 E. Ising, Z. Phys. **31**, 253 (1925)
2 N.D. Mermin, H. Wagner, Phys. Rev. Lett. **17**, 1133 (1966)
3 P. Bruno, Phys. Rev. Lett. **87**, 137 203 (2001)
4 L.J. de Jongh, A.R. Miedema, Adv. Phys. **23**, 1 (1974)
5 D.W. Hone, P.M. Richards, Annu. Rev. Mater. Sci. **4**, 337 (1974)
6 R. Dingle, M.E. Lines, S.L. Holt, Phys. Rev. **187**, 643 (1969)
7 C.P. Landee, R.D. Willett, Phys. Rev. Lett. **43**, 463 (1979)
8 C. Dupas, J.P. Renard, J. Seiden, A. Cheikh-Rouhou, Phys. Rev. B **25**, 3261 (1982)

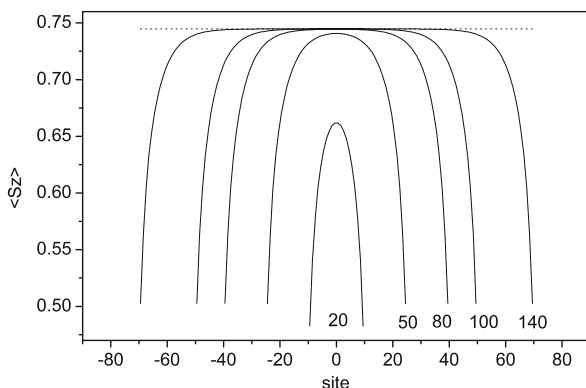9 A. Caneschi, D. Gatteschi, N. Lalioti, C. Sangregorio, R. Sessoli, G. Venturi, A. Vindigni, A. Rettori, M.G. Pini, M.A. Novak, Angew. Chem. Int. Edit. **40**, 1760 (2001)

10 L. Bogani, A. Caneschi, M. Fedi, D. Gatteschi, M. Massi, M.A. Novak, M.G. Pini, A. Rettori, R. Sessoli, A. Vindigni, Phys. Rev. Lett. **92**, 207204 (2004)

11 R. Clerac, H. Miyasaka, M. Yamashita, C. Coulon, J. Am. Chem. Soc. **124**, 12837 (2002)

12 R. Lescouëzec, J. Vaissermann, C. Ruiz-Pérez, F. Lloret, R. Carrasco, M. Julve, M. Verdaguer, Y. Dromzee, D. Gatteschi, W. Wernsdorfer, Angew. Chem. Int. Edit. **42**, 1483 (2003)

13 R.J. Glauber, J. Math. Phys. **4**, 294 (1963)

14 F.J. Himpsel, J.E. Ortega, G.J. Mankey, R.F. Willis, Adv. Phys. **47**, 511 (1998) and references therein

15 H.J. Elmers, J. Hauschild, H. Höche, U. Gradmann, H. Bethge, D. Heuer, U. Köhler, Phys. Rev. Lett. **73**, 898 (1994)

16 J. Shen, R. Skomski, M. Klaua, H. Jenniches, S. Sundar Manoharan, J. Kirschner, Phys. Rev. B **56**, 2340 (1997)

17 J. Shen, M. Klaua, P. Ohresser, H. Jenniches, J. Barthel, C.V. Mohan, J. Kirschner, Phys. Rev. B **56**, 11134 (1997)

18 J. Hauschild, H.J. Elmers, U. Gradmann, Phys. Rev. B **57**, R677 (1998)

19 P. Ohresser, G. Ghiringhelli, O. Tjernberg, N.B. Brookes, Phys. Rev. B **62**, 5803 (2000)

20 D. Li, B. Roldan Cuenya, J. Pearson, S.D. Bader, W. Keune, Phys. Rev. B **64**, 144410 (2001)

21 M. Pratzer, H.J. Elmers, M. Bode, O. Pietzsch, A. Kubetzka, R. Wiesendanger, Phys. Rev. Lett. **87**, 127201 (2001)

22 P. Gambardella, M. Blanc, L. Bürgi, K. Kuhnke, K. Kern, Surf. Sci. **449**, 93 (2000)

23 P. Gambardella, A. Dallmeyer, K. Maiti, M.C. Malagoli, W. Eberhardt, K. Kern, C. Carbone, Nature **416**, 301 (2002)

24 P. Gambardella, J. Phys.: Condens. Matter **15**, S2533 (2003)

25 P. Gambardella, A. Dallmeyer, K. Maiti, M.C. Malagoli, S. Rusponi, P. Ohresser, W. Eberhardt, C. Carbone, K. Kern, Phys. Rev. Lett. **93**, 077203 (2004)

26 N.W.E. McGee, M.T. Johnson, J.J. de Vries, J. aan de Stegge, J. Appl. Phys. **73**, 3418 (1993)

27 P. Gambardella, M. Blanc, H. Brune, K. Kuhnke, K. Kern, Phys. Rev. B **61**, 2254 (2000)

28 B.T. Thole, P. Carra, F. Sette, G. van der Laan, Phys. Rev. Lett. **68**, 1943 (1992)

29 C.T. Chen, Y.U. Idzerda, H.-J. Lin, N.V. Smith, G. Meigs, E. Chaban, G.H. Ho, E. Pellegrin, F. Sette, Phys. Rev. Lett. **75**, 152 (1995)

30 P. Carra, B.T. Thole, M. Altarelli, X. Wang, Phys. Rev. Lett. **70**, 694 (1993)

31 R. Wu, A.J. Freeman, Phys. Rev. Lett. **73**, 1994 (1994)

32 M. Komelj, C. Ederer, J.W. Davenport, M. Fähnle, Phys. Rev. B **66**, 140407(R) (2002)

33 J. Hong, R.Q. Wu, Phys. Rev. B **70**, 060406 (2004)

34 C. Ederer, M. Komelj, M. Fähnle, Phys. Rev. B **68**, 012407 (2003)

35 B. Lazarovits, L. Szunyogh, P. Weinberger, Phys. Rev. B **67**, 024415 (2003)

36 J. Hong, R.Q. Wu, Phys. Rev. B **67**, 020406(R) (2003)

37 B. Újfalussy, B. Lazarovits, L. Szunyogh, G.M. Stocks, P. Weinberger, Phys. Rev. B **70**, 100404 (2004)

38 A.B. Shick, F. Máca, P.M. Oppeneer, Phys. Rev. B **69**, 212410 (2004)

39 A. Dallmeyer, C. Carbone, W. Eberhardt, C. Pampuch, O. Rader, W. Gudat, P. Gambardella, K. Kern, Phys. Rev. B **61**, R5133 (2000)

40 J. Dorantes-Dávila, G.M. Pastor, Phys. Rev. Lett. **81**, 208 (1998)

41 L. Zhou, D. Wang, Y. Kawazoe, Phys. Rev. B **60**, 9545 (1999)

42 R. Félix-Medina, J. Dorantes-Dávila, G.M. Pastor, New J. Phys. **4**, 100 (2002)

43 M. Weinert, A.J. Freeman, J. Magn. Magn. Mater. **38**, 23 (1983)

44 D. Spišák, J. Hafner, Phys. Rev. B **67**, 134434 (2003)

45 M. Pratzer, H.J. Elmers, Phys. Rev. B **67**, 094416 (2002)

46 S. Ferrer, J. Alvarez, F. Lundgren, X. Torrelles, P. Fajardo, F. Boscherini, Phys. Rev. B **56**, 9848 (1997)

47 U. Gradmann, *Handbook of Magnetic Materials*, vol. 7/1, ed. by K.H.J. Buschow (Elsevier, Amsterdam, 1993), pp. 1–96

48 D. Sander, J. Phys.: Condens. Matter **16**, R603 (2004)

49 P. Gambardella, S. Rusponi, M. Veronese, S.S. Dhesi, C. Grazioli, A. Dallmeyer, I. Cabria, R. Zeller, P.H. Dederichs, K. Kern, C. Carbone, H. Brune, Science **300**, 1130 (2003)

50 M. Blume, P. Heller, N.A. Lurie, Phys. Rev. B **11**, 4483 (1975)

51 R. Pandit, C. Tannous, Phys. Rev. B **28**, 281 (1982)

52 M. Wortis, Phys. Rev. B **10**, 4665 (1974)

53 M.G. Pini, A. Rettori, Phys. Lett. A **127**, 70 (1988)

54 M.G. Pini, A. Rettori, in *Fundamental and Applicative Aspects of Disordered Magnetism*, ed. by P. Allia, D. Fiorani, L. Lanotte (World Scientific, Singapore, 1989), pp. 1–29 and references therein

55 H.E. Stanley, *Introduction to Phase Transitions and Critical Phenomena* (Clarendon, Oxford, 1971)

56 A.H. Stroud, *Approximate Calculation of Multiple Integrals* (Prentice Hall, Englewood Cliffs, NJ, 1971)

57 http://www.netlib.org/lapack/

58 M. Abramowitz, I.E. Stegun, *Handbook of Mathematical Functions* (Dover, New York, 1970)

59 M.E. Fisher, Am. J. Phys. **32**, 343 (1964)

60 Equations (18) and (22) are slightly different when surface spins are involved: e.g. for the magnetization one has $\langle S_1^\alpha \rangle = \langle S_N^\alpha \rangle = (1/\mathcal{Z}_N) \sum_n \lambda_n^{N-1} a_n f_n$, where $f_n = \int S_i^\alpha \psi_n(\mathbf{S}_i) \mathrm{d}\Omega_i$.

61 S. Ruttinger, H. Magnan, H. Wende, P. Le Fevre, K. Baberschke, D. Chandesris, Surf. Sci. **548**, 138 (2004)

62 M. van Schilfgaarde, V.P. Antropov, J. Appl. Phys. **85**, 4827 (1999)

63 S. Frôta-Pessoa, R.B. Munizand, J. Kudrnovský, Phys. Rev. B **62**, 5293 (2000)

64 M. Pajda, J. Kudrnovský, I. Turek, V. Drchal, P. Bruno, Phys. Rev. Lett. **85**, 5424 (2000)

65 M. Pratzer, H.J. Elmers, Phys. Rev. B **67**, 094416 (2003)

66 D. Hinzke, U. Nowak, Phys. Rev. B **61**, 6734 (2000)

67 H.-B. Braun, Phys. Rev. B **50**, 16501 (1994)

68 H.-B. Braun, J. Appl. Phys. **85**, 6172 (1999)